The Astrophysical Journal, 889:30 (10pp), 2020 January 20 https://doi.org/10.3847/1538-4357/ab5fda

Two-zone Spatially Dependent Model of the Nonthermal Emission from Plerionic Supernova Remnant G21.5-0.9

Fang-Wu Lu[1,2], Quan-Gui Gao[1,2], and Li Zhang[2]
[1] Department of Physics, Yuxi Normal University, Yuxi 653100, People's Republic of China; lizhang@ynu.edu.cn
[2] Department of Astronomy, Key Laboratory of Astroparticle Physics of Yunnan Province, Yunnan University, Kunming 650091, People's Republic of China
Received 2019 September 1; revised 2019 December 2; accepted 2019 December 6; published 2020 January 22

Abstract

Observations of plerionic supernova remnant (SNR) G21.5-0.9 indicate an extended X-ray halo surrounding the bright central pulsar wind nebula (PWN), and that the photon index and the surface brightness of the SNR have been discovered to change with the increase of radial distance in the X-ray band. To explain the observational features of this source, a two-zone spatially dependent model with a slow diffusion in the PWN and a fast diffusion in the extended region is proposed in this paper. In the model, the evolution of electron inside the entire remnant is described with a particle transport equation under the assumption of a spherically symmetric system with dynamical evolution. The observed photon spectral energy distribution of the central PWN, as well as the radial profiles of the photon index and surface brightness observed in the X-ray band of the entire remnant, can be well reproduced in the framework of the model. The modeling results reveal that the X-ray halo of SNR G21.5-0.9 is mainly due to the synchrotron radiation of the accelerated electrons derived from the PWN shock, and the current diffusion coefficient in the extended region has a value of $1.7 \times 10^{28}\,\mathrm{cm^2\,s^{-1}}$ at an electron energy of 1 TeV, which is much larger than the obtained spatial averaged diffusion coefficient of $2.5 \times 10^{25}\,\mathrm{cm^2\,s^{-1}}$ in the central nebula.

Unified Astronomy Thesaurus concepts: Interstellar medium (847); Supernova remnants (1667); Pulsars (1306)

1. Introduction

A rotation-powered pulsar loses most of its rotational energy through a relativistic magnetized outflow usually referred to as a pulsar wind (e.g., Goldreich & Julian 1969; Kennel & Coroniti 1984a). The collision of the pulsar wind with the ambient supernova (SN) ejecta and/or interstellar material (ISM) results in a termination shock (TS) and creates a pulsar wind nebula (PWN; Rees & Gunn 1974; Reynolds & Chevalier 1984). The particles of the pulsar wind can be accelerated to extreme relativistic energy at the TS and then injected into the PWN and emit photons ranging from radio, X-ray to TeV γ-ray bands (e.g., Kennel & Coroniti 1984b; de Jager & Harding 1992; Atoyan & Aharonian 1996). Many PWNe, such as 3C58, G21.5-0.9, G29.7-0.3, MSH 15-52, Vela X, and HESS J1825-137, have been spatially resolved in the radio, X-ray, and even TeV γ-ray bands, which provide basic information to study pulsar winds, particle acceleration, and evolution of the magnetic field as well as particle transport.

G21.5-0.9 is a composite, young plerionic supernova remnant (SNR) that shows a bright, highly spherical central PWN and a faint X-ray halo (Slane et al. 2000; Safi-Harb et al. 2001). The photons emitting from the bright central PWN have been detected at radio, infrared, X-ray, and TeV γ-ray bands. In the radio band, the central PWN was detected to have a power-law spectrum with a flat spectral index of $\alpha \sim 0.1$ and an elliptical brightness distribution which is peaked near the geometric center of the remnant (e.g., Becker & Kundu 1976; Wilson & Weiler 1976). Based on the *Chandra* X-ray observations, the total flux of the central PWN in the 0.5–10 keV energy range was reported to have a value of $7.0 \times 10^{-11}\,\mathrm{erg\,s^{-1}\,cm^{-2}}$ with a power-law photon index of 1.91 ± 0.4 (Slane et al. 2000). More importantly, the photon index and the surface brightness of the central nebula have been discovered to change with the increase of radial distance in the X-ray band (e.g., Slane et al. 2000; Matheson & Safi-Harb 2005). According to the H.E.S.S. observations, the photon spectrum of the central PWN can be well described by a power-law with a photon index of 2.08 ± 0.22 in the 0.2–4 TeV energy range (Djannati-Ataï et al. 2008).

G21.5-0.9 was the first PWN that has been discovered to be surrounded by a faint nonthermal X-ray halo (Slane et al. 2000). The X-ray properties of the entire remnant of G21.5-0.9 was spatially resolved with the *Chandra* observed data (Matheson & Safi-Harb 2005), in which the photon index of the SNR steepens with the increasing radial distance from the center of the PWN to the edge of 40″ and then becomes constant at ∼2.4 within the X-ray halo out to a radius of 150″. Recently, it has been confirmed that the extended halo was dominated by the nonthermal X-rays and found that the photon index of the X-ray spectrum continues to rise beyond the edge of the PWN at 40″, which reaches a maximum at 50″ and remains roughly flat to the edge of the remnant (Guest et al. 2019).

It is generally believed that the radio and X-rays of the central PWN of SNR G21.5-0.9 are produced by synchrotron radiation of the relativistic electrons injected from the TS, and the γ-rays are mainly from the inverse Compton (IC) scattering of various soft photons inside the central nebula (e.g., Zhang et al. 2008; Tanaka & Takahara 2011; Vorster et al. 2013; Torres et al. 2014; Zhu et al. 2018). Moreover, the spatially radiative properties of the X-rays of the central PWN have been extensively studied in the framework of the particle transport models (e.g., Tang & Chevalier 2012; Porth et al. 2016; Lu et al. 2017b). The modeling results revealed that particle diffusion is important for modifying the photon index of the X-rays. For the nonthermal X-ray halo of G21.5-0.9, there are three possible interpretations, i.e., a nonthermal shell formed by the interaction of the blast wave with the surrounding medium (Slane et al. 2000), an extension of the central nebula (Safi-

Harb et al. 2001; Warwick et al. 2001), and the dust scattering of the X-rays from the central PWN (Bocchino et al. 2005).

In this paper, a two-zone spatially dependent model is presented to investigate the nonthermal radiative properties of SNR G21.5-0.9, including the spectral energy distribution (SED) of the central PWN as well as the radial profiles of the photon index and surface brightness in the X-ray band of the entire remnant. In the model, the particle diffusion in the PWN is assumed to be smaller than that in the extended region according to Abeysekara et al. (2017), and the particles in the extended region are considered to be originated from the central nebula and the PWN shock. Furthermore, the organization of the paper is as follows. In Section 2, the description of the two-zone spatially dependent model is given. In Section 3, the modeling results of G21.5-0.9 are presented. Finally, the main conclusions and discussions are given in Section 4.

2. The Model

For a composite SNR, its structure usually retains spherical symmetry during the early stage of evolution (e.g., Slane et al. 2000). As the SN ejecta expands into the ambient ISM, two shocks are produced, i.e., a forward shock propagates into the surrounding ISM and a reverse shock propagates back into the gas of ejecta, which results in an expanding shell composed of heated ejecta (e.g., McKee 1974; Truelove & McKee 1999). At the same time, a PWN that powered by the central pulsar through its relativistic magnetized wind evolves in the interior of the expanding SNR. The PWN expands supersonically and derives a PWN shock into the ambient ejecta, and then heating the ejecta and producing thermal emission. The properties of the PWN shock, such as the temperature of the shocked ejecta and the radius and velocity of the shock, depending on the spin-down power of the central pulsar and the density and velocity profiles of the surrounding ejecta (e.g., Kolb et al. 2017; Slane 2017). According to the hydrodynamical simulations, the heated ejecta swept up by the PWN shock can be collected in a thin shell and the thickness of the shell is about $1/24$ of the radius of the shock (e.g., Blondin et al. 2001; van der Swaluw et al. 2001; Bucciantini et al. 2003). In the region between the PWN shock and the reverse shock of the SNR, the expanding ejecta of the supernova progenitor have not been shocked. The schematic structure of such a young composite SNR is presented in Figure 1.

In the present work, the photon emission from the thin shell derived by the PWN shock is neglected, due to the thickness of the shell is much smaller than the radius of the central nebula (e.g., van der Swaluw et al. 2001), and our interests are focused on the photon emission from the central PWN and the extended halo. Moreover, we notice that as the SN ejecta propagates into a low-density medium, the SNR shell of the composite SNR would be very faint (e.g., Slane et al. 2000). In this case, the photon emission from the SNR shell is also unimportant. Thus, in our two-zone model, a composite SNR is assumed to be a spherically symmetric system with two regions of particle's production and diffusion: the PWN powered by the central pulsar (called as a PWN and labeled as region I) and the region between the PWN and the SNR (called as an extended region and labeled as region II). These two regions have a diffusion boundary located at the edge of the PWN and different diffusion coefficients (see Figure 1).

In the region I, the particles are injected from the TS which is formed by the interaction of the pulsar wind with the ambient SN ejecta, and the evolution of the particle spectrum can be described by the Fokker–Planck transport equation (e.g., Ginzburg & Syrovatskii 1964; Parker 1965)

$$\frac{\partial n_{\rm e}}{\partial t} = \kappa\frac{\partial^2 n_{\rm e}}{\partial r^2} + \left[\frac{1}{r^2}\frac{\partial}{\partial r}(r^2\kappa) - V\right]\frac{\partial n_{\rm e}}{\partial r} - \frac{1}{r^2}\frac{\partial}{\partial r}[r^2 V]n_{\rm e} + \frac{\partial}{\partial \gamma}[\dot{\gamma} n_{\rm e}] + Q_{\rm inj}, \tag{1}$$

where $n_{\rm e} = n_{\rm e}(\gamma, r, t)$ is the differential number density of the electron at a radial position of r, γ is the Lorentz factor of electrons, $\dot{\gamma}$ is the total energy losses due to adiabatic expansion, synchrotron radiation and IC scattering, and $Q_{\rm inj}$ represents the particles injected from the central pulsar. Furthermore, $\kappa = \kappa(r, \gamma, t)$ and $V = V(r)$ represent the diffusion coefficient and convection velocity of the particles, respectively.

According to the two-dimensional particle-in-cell simulations of Spitkovsky (2008), the distribution of particles in the downstream of the TS can be described as a Maxwellian plus with a power-law tail, i.e.,

$$Q_{0,\rm inj}(\gamma, t) = \begin{cases} Q_{0,\rm S1}(t)\frac{\gamma}{\gamma_{\rm b}}\exp\left(-\frac{\gamma}{\Delta\gamma}\right) \\ Q_{0,\rm S2}(t)\left(\frac{\gamma}{\gamma_{\rm b}}\right)^{-\alpha} \\ Q_{0,\rm S2}(t)\left(\frac{\gamma}{\gamma_{\rm b}}\right)^{-\alpha}\exp\left(-\frac{\gamma-\gamma_{\rm cut}}{\Delta\gamma_{\rm cut}}\right) \end{cases}, \tag{2}$$

for $\gamma \leqslant \gamma_{\rm max}$, $\gamma_b < \gamma \leqslant \gamma_{\rm cut}$ and $\gamma_{\rm cut} < \gamma \leqslant \gamma_{\rm max}$ in the three respective equations. In the above equation, $\gamma_{\rm b}$, $\Delta\gamma$, $\gamma_{\rm cut}$, $\Delta\gamma_{\rm cut}$, and $\gamma_{\rm max}$ are the break, Maxwellian spread, cut-off, cut-off spread, and maximum Lorentz factors of the accelerated electrons, respectively. The terms $Q_{0,\rm S1}(t)$ and $Q_{0,\rm S2}(t)$ are the time dependent normalization constants that are determined by $(1-\eta_{\rm B})L(t) = \int_0^\infty \gamma m_{\rm e}c^2 Q_{0,\rm inj}(\gamma, t)d\gamma$, where $L(t)$ is the spin-down luminosity of a pulsar and $\eta_{\rm B}$ is the fraction of the spin-down luminosity converted into magnetic energy. Since the number of particles that flow through the TS should be equal to the injected particles, the inner boundary condition, which is located at the shock, can be expressed as

$$V_0 n_{\rm e} - \kappa(r_0, \gamma, t)\frac{\partial n_{\rm e}}{\partial r} = \frac{Q_{0,\ \rm inj}(\gamma, t)}{4\pi r_0^2}, \tag{3}$$

where $r_0 = R_{\rm ts}(t)$ is the radius of the TS at time t and V_0 is the convection velocity of the particles at the TS.

Under the assumption that the pulsar is a pure dipole radiator, the evolution of the spin-down luminosity of a pulsar can be given by (e.g., Pacini & Salvati 1973; Gaensler & Slane 2006)

$$L(t) = L_0\left(1 + \frac{t}{\tau_0}\right)^{-\frac{n+1}{n-1}}, \tag{4}$$

where L_0 is the initial luminosity, n is the braking index, and τ_0 is the initial spin-down timescale that is calculated by $\tau_0 = 2\tau_{\rm c}/(n-1) - T_{\rm age}$, with $\tau_{\rm c}$ and $T_{\rm age}$ are the characteristic

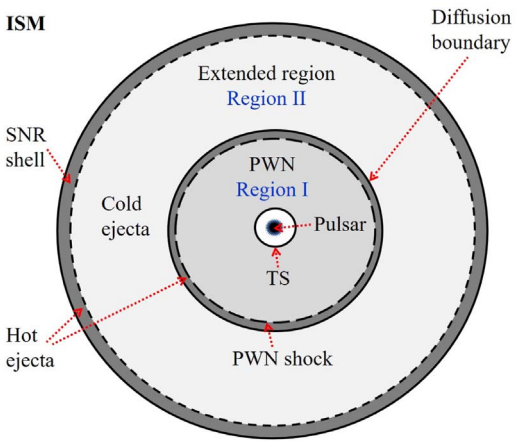

Figure 1. Schematic illustration of our two-zone model. The inner part of the SNR (labeled as region I) corresponds to the PWN that powered by the central pulsar and the particles are injected from the TS. The outer part composed of cold ejecta (labeled as region II) of the SNR is the extended region dominated by the particles originated from the central PWN and the PWN shock.

age and the age of the pulsar, respectively. As the Larmor radius of the accelerated particles must be less than the radius of the TS, the maximum energy of the accelerated particles can be calculated by $\gamma_{\rm max} = 3\varepsilon e\sqrt{\eta_{\rm B}L(t)/c}\,/m_{\rm e}c^2$, where ε is the ratio of Larmor radius to the TS radius and e is the electron charge. In this paper, the value of ε is adopted to be 0.2 according to Torres et al. (2014).

Based on the one-dimensional magnetohydrodynamical (MHD) simulations of Kennel & Coroniti (1984a), a toroidal magnetic field in the PWN is adopted in this paper. The evolution of the magnetic field in the region I can be described as (Lu et al. 2017a)

$$B(r,\,t) = B_0(t)\left[\frac{r_0}{rv(r)}\right], \tag{5}$$

where $v(r)$ is the radial profile of the convection velocity and $B_0(t)$ is the magnetic field at the TS that is calculated with (e.g., Pacini & Salvati 1973)

$$\frac{dW_{\rm B}(t)}{dt} = \eta_{\rm B}L(t) - \frac{W_{\rm B}(t)}{R_{\rm pwn}(t)}\frac{dR_{\rm pwn}(t)}{dt}. \tag{6}$$

In the above equation, $W_{\rm B}(t) = \int_{R_{\rm ts}(t)}^{R_{\rm pwn}(t)} B^2(r,\,t)r^2dr/2$ is the magnetic energy, and $R_{\rm pwn}(t)$ is the radius of the PWN. Note that the magnetic fields would be amplified by the PWN shock at the outer boundary of the nebula (e.g., Bamba et al. 2003; Vink & Laming 2003; Reynolds et al. 2012), and the magnetic bubble should extend to the whole extended region outside the boundary. Due to the conservation of the magnetic field flux, the magnetic field in the extended region could be different from that in the central nebula, i.e., a lower magnetic field in the region II is expected. In this paper, the magnetic field in the region II is assumed to be spatially independent and its evolution of the time is the same as that in the region I. Thus, the magnetic field in region II can be given by $B_{\rm snr}(t) = \xi B_{\rm pwn}(t)$, where ξ is the ratio of the magnetic field in the region II to that at the edge of the nebula and $B_{\rm pwn}(t)$ is the magnetic field at the edge of the central PWN. Moreover, the convection velocity of the particles inside the region I is calculated by $V(r) = V_0 v(r)$. It should be noted that the MHD simulations of Kennel & Coroniti (1984a) also revealed that the velocity decreases with the increase of radial distance and approaches a constant in the outer region of the nebula and that the value is much smaller than that at the inner region. Thus, in the present work, the convection of particles inside the extended region is neglected, i.e., the propagation of particles in the region II is considered to be diffusion dominated.

Recently, a possible explanation for the HAWC observations of Geminga and PSR B0656+14 pulsar was suggested: the electron–positron pairs around these sources diffuse out significantly slower than those in the surrounding ISM (Abeysekara et al. 2017). In our model, the diffusion coefficient in the region I is also assumed to be smaller than that in the region II, and the particle diffusion is expressed as $\kappa = \kappa_0\kappa_{\rm r}\kappa_\gamma$ with κ_0 is a constant (Lerche & Schlickeiser 1981). It is generally believed that particle diffusion results from particles interacting with irregularities in the magnetic field. As a toroidal magnetic field in the PWN is adopted in our model, the diffusion necessarily occurs perpendicular to the magnetic field, where the diffusion of particle across the magnetic field lines is expected to be small (e.g., de Jager & Djannati-Ataï 2009). However, even a small amount of cross field transport could result in an unneglectable mixing (Tang & Chevalier 2012). Thus, the radial diffusion should be considered. Furthermore, the radial dependence of the diffusion can be modeled as $\kappa_{\rm r} \propto 1/B(r,\,t)$ according to Caballero-Lopez et al. (2004), and the energy dependence is given by $\kappa_\gamma \propto \gamma^\delta$ with $\delta = 0.333$ (Aguilar et al. 2016). Therefore, the diffusion coefficient of the two-zone model can be given by

$$\kappa(r,\,\gamma,\,t) = \begin{cases}\kappa_1(r,\,\gamma,\,t) & r < R_{\rm pwn}(t)\\ \kappa_2(r,\,\gamma,\,t) & r \geqslant R_{\rm pwn}(t)\end{cases}, \tag{7}$$

where

$$\kappa_1(r,\,\gamma,\,t) = \kappa_{0,1}(t)\left[\frac{\gamma m_{\rm e}c^2}{1\ {\rm TeV}}\right]^\delta\left[\frac{rv(r)}{r_0}\right], \tag{8}$$

is the diffusion coefficient in the region I and

$$\kappa_2(r,\,\gamma,\,t) = \kappa_{0,2}(t)\left[\frac{\gamma m_{\rm e}c^2}{1\ {\rm TeV}}\right]^\delta, \tag{9}$$

is the diffusion coefficient in the region II. Note that the diffusion coefficient in the region II is spatially independent because the magnetic field is assumed to be spatially independent in our model.

For the particles in the region II, in addition to the particles diffuse from the central nebula, the particles injected from the PWN shock are also considered. Following the hydrodynamical simulations of Slane (2017), a PWN shock is formed in the interaction of the expanding nebula with the ambient SN ejecta, where the properties of the shock depend on the expanding velocity of the PWN and the density distribution of the ejecta. For a strong shock, the swept-up particles including electrons and protons can be accelerated to very high energy. At the shock, the accelerated particles would be diffused into region II and then emit photons via synchrotron radiation and IC scattering of electrons, as well as π^0 decay in the proton-proton interaction of energetic nucleons with the ambient medium, where the photon spectrum is determined by the magnetic field, the distribution of particles in the region II and the density of

the ambient gas. According to the diffusive shock acceleration calculations, the distribution of the accelerated particles injected from the shock depends on the shock compression ratio, gas density, fluid velocity, and spatial diffusion coefficient (e.g., Kang et al. 2009; Vladimirov et al. 2009; Caprioli et al. 2010a, 2010b). Here, the nonthermal X-rays of region II are considered to be mainly from the synchrotron radiation of the accelerated electrons, due to the hadronic contribution to the photon spectrum is mainly on the γ-rays. The spectrum of the accelerated particles at the PWN shock is assumed to be described by the power-law with an exponential cut-off function,

$$Q_{1,\mathrm{inj}} = Q_{0,\mathrm{e}}\gamma^{-\beta}\exp\left(-\frac{\gamma}{\gamma_{\mathrm{e,cut}}}\right)H(\gamma-\gamma_{\mathrm{e,min}}). \quad (10)$$

This energy distribution is expected in the downstream region of the PWN shock with particles suffering from energy losses (e.g., Fang et al. 2009; Acero et al. 2010; Zeng et al. 2017). In the above equation, $Q_{0,\mathrm{e}}$ is the normalization constant, β, $\gamma_{\mathrm{e,min}}$, and $\gamma_{\mathrm{e,cut}}$ are the spectral index, minimum, and cut-off energy of the accelerated electrons, respectively, which are dependent on the nature of the PWN shock and the density of the ambient medium. In this paper, these quantities are treated as free parameters for simplicity. The term H is the Heaviside function which is defined as: $H(x) = 0$ for $x < 0$ and $H(x) = 1$ for $x \geqslant 0$. To further simplify the model, the accelerated particles are assumed to be injected from the edge of the PWN. Because the number of particles that flow through the edge of the PWN should be equal to the injected particles originated from the central nebula and the PWN shock, the diffusion boundary condition can be expressed as

$$\frac{Q_{1,\mathrm{inj}}(\gamma)}{4\pi r_{\mathrm{b}}^2} + \kappa_1(r_{\mathrm{b}},\gamma,t)\frac{\partial n_{\mathrm{e}}}{\partial r} = \kappa_2(r_{\mathrm{b}},\gamma,t)\frac{\partial n_{\mathrm{e}}}{\partial r}, \quad (11)$$

where $r_{\mathrm{b}} = R_{\mathrm{pwn}}(t)$ is the boundary between the PWN and the extended region. The particles in the extended region should lose energy due to the expansion of the ejecta. In this model, the convection velocity is neglected for the propagation of the particles in the region II, which is considered to be diffusion dominated. Thus, the evolution of the particle spectrum in region II is also described by the Fokker–Planck transport Equation (1) except for the convection of the particles is neglected.

In our model, the dynamical evolutions of the SNR and the PWN are simulated with the models of Truelove & McKee (1999) and Bucciantini et al. (2011), where the mass and energy of the progenitor SN ejects are respectively assumed to be M_{ej} and E_{sn}, and the number density of the ambient matter is considered with a constant of ρ_{ism}. In our numerical treatments, the dynamical radii of the PWN and the SNR, as well as the electron spectra of the entire remnant at different positions, can be obtained through numerically solving the dynamical and particle transport equations simultaneously, and then the photon spectra of the remnant can be calculated for the processes of synchrotron radiation and IC scattering of the various soft photons (e.g., de Jager & Harding 1992; Atoyan & Aharonian 1996; Volpi et al. 2008). Finally, the surface brightness and the photon index, in the different energy bands at different positions, can be calculated with the scenario of Holler et al. (2012).

3. Results

3.1. Application to SNR G21.5-0.9

The two-zone model described in Section 2 is now applied to the composite SNR G21.5-0.9. The radio observations revealed that the central PWN of G21.5-0.9 is powered by the central pulsar PSR J1833-1034, which has a period of $P = 61.86$ ms, a period derivative of $\dot{P} = 2.02 \times 10^{-13}$ s s^{-1} and a characteristic age of $\tau_{\mathrm{c}} = 4860$ yr (Camilo et al. 2006). According to the measured expansion rate of the central PWN in the radio band, the age of PSR J1833-1034 is estimated to be 870 yr (Bietenholz & Bartel 2008). Based on H I and CO measurements, Camilo et al. (2006) reported that the distance to the system has a value of 4.7 ± 0.4 kpc. In this paper, the distance is adopted to be 5 kpc according to Guest et al. (2019). The braking index for the pulsar is generally adopted to be $n = 3$ under the assumption that the pulsar is a purely rotating magnetic dipole (e.g., Tanaka & Takahara 2011; Torres et al. 2014; Lu et al. 2017b).

3.1.1. Photon SEDs

The dynamical radii and photon SEDs of SNR G21.5-0.9, including the time evolution of the radius of the TS (R_{ts}), PWN (R_{pwn}), reverse shock (R_{rs}) and forward shock (R_{snr}), as well as the photon spectra of the central PWN and the extended region, calculated in the framework of our model, are shown in Figure 2. In the calculations, the adopted parameters are listed in Table 1. The soft photon fields involved in the IC scattering of the central PWN are as follows: the cosmic microwave background (CMB; temperature 2.73 K, photon density 0.26 eV cm^{-3}), the galactic far-infrared background (FIR; temperature 35 K, photon density 5.4 eV cm^{-3}), and the near-infrared and optical photon field due to the stars (NIR; temperature 3500 K, photon density 5.0 eV cm^{-3}). In the extended region, the target photon field is only the CMB.

As seen in the left panel of Figure 2, region I of the two-zone model corresponds to the region between the TS and the outer boundary of the central PWN, while region II is located between the PWN and the forward shock. It should be pointed out that, although the models of Bucciantini et al. (2011) and Truelove & McKee (1999) can account for the time evolutions of the dynamical radii of SNR G21.5-0.9, the nature of the entire remnant, e.g., the radial profile of the gas density, does not be considered. Thus, a hydrodynamical model which involves the evolution of the gas density should be introduced in the two-zone model to investigate the dynamical evolution of the SNR more precisely (e.g., Blondin et al. 2001; van der Swaluw et al. 2001; Bucciantini et al. 2003; Slavin et al. 2017), while it is out of the scope of this paper.

It can be seen from the right panel of Figure 2 that the observed photon SED of the central PWN can be well reproduced in the framework of our model except for the observations in the infrared band. Similarly to the one-zone spatially dependent model results of Lu et al. (2017b), it is found that any set of appropriate parameters cannot reproduce the observed data of the central PWN in the infrared band. The photon SED of the extended region calculated with our model reveals that the spectral flux of the extended region is lower than that of the central nebula in the X-ray and γ-ray bands.

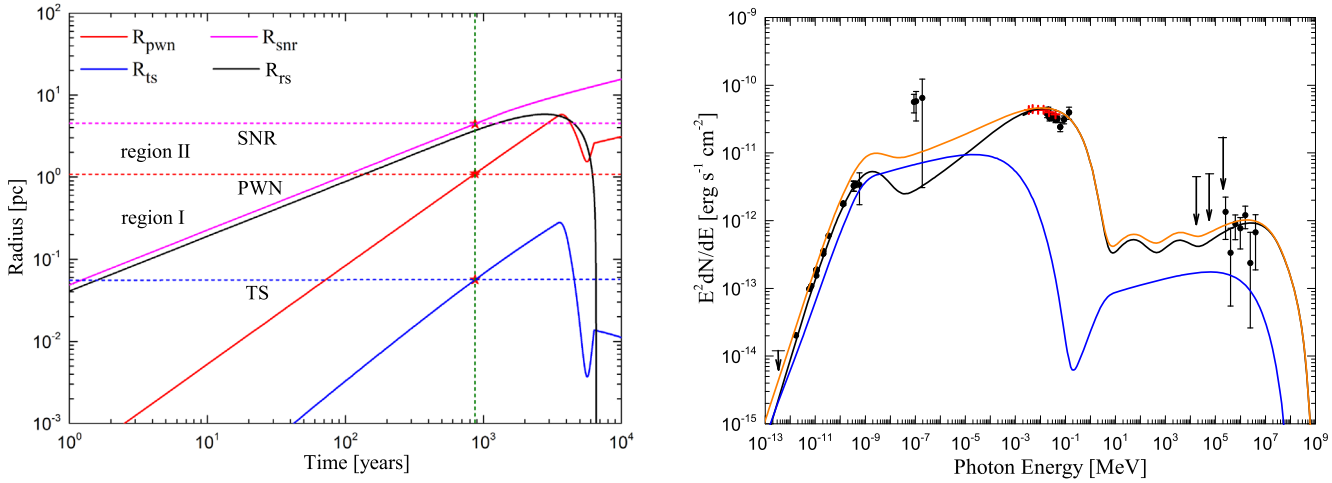

Figure 2. Left panel: time evolution of the radius of the forward shock ($R_{\rm snr}$, magenta line), reverse shock ($R_{\rm rs}$, black line), PWN ($R_{\rm pwn}$, red line), and TS ($R_{\rm ts}$, blue line). The vertical dashed line indicates the evolutions of G21.5-0.9 at the current age of 870 yr. Right panel: comparison of the modeling results of G21.5-0.9 with the observations of the central PWN. The black and blue lines are the fluxes of the PWN and the extended region, respectively. The orange line is the spectral flux of the entire remnant. The observed data of the central nebula are taken from Salter et al. (1989) (radio), Gallant & Tuffs (1998) (infrared), de Rosa et al. (2009), Tsujimoto et al. (2011) and Nynka et al. (2014) (X-rays), Djannati-Ataï et al. (2008), Gallant et al. (2008) and Acero et al. (2013) (γ-rays).

Table 1
Values of the Parameters used to Reproduce the Current Observations of G21.5-0.9

Parameter	Value	Parameter	Value
$E_{\rm SN}$	1.0×10^{51} erg	$\eta_{\rm B}$	0.005
$M_{\rm ej}$	$5.0\,M_{\odot}$	α	2.2
$\rho_{\rm ism}$	0.3 cm^{-3}	$\Delta\gamma$	2.0×10^{4}
P	61.86 ms	$\gamma_{\rm b}$	1.4×10^{5}
$\dot{P}$	2.02×10^{-13} s $\cdot$ s^{-1}	$\Delta\gamma_{\rm cut}$	3.0×10^{8}
L_0	1.58×10^{38} erg s^{-1}	$\gamma_{\rm cut}$	9.0×10^{8}
$\tau_{\rm c}$	4860 yr	ξ	0.64
τ_0	3990 yr	β	2.5
n	3.0	$\gamma_{\rm e,min}$	4.0×10^{4}
$Q_{0,\ e}$	4.5×10^{46} s^{-1}	$\gamma_{\rm e,cut}$	5.5×10^{7}
$\kappa_{0,1}$	4.1×10^{21} cm^2 s^{-1}	$T_{\rm age}$	870 yr
$\kappa_{0,2}$	1.2×10^{24} cm^2 s^{-1}	d	5.0 kpc

However, the flux of the extended region is higher than the spectral flux of the central PWN in the infrared band, because the particles injected from the PWN shock is considered in our model.

3.1.2. Radial Profiles of the X-Rays

The *Chandra* X-ray observations found that the photon index and the surface brightness of the central PWN of SNR G21.5-0.9 in the X-ray band have obvious changes as the increase of the radial distance, i.e., the photon index steepens with the radial distance and the surface brightness decrease with the increase of the radial distance (e.g., Slane et al. 2000; Safi-Harb et al. 2001; Matheson & Safi-Harb 2005). According to the parameters listed in Table 1, the radial profiles of the X-rays of the central nebula calculated in our model are shown in Figure 3. The observed data of the radial photon index and surface brightness of the central PWN in the X-ray band given by Guest et al. (2019) can be well reproduced in the framework of our model.

According to the deeper *Chandra* X-ray observations, the surface brightness of the extended region in the X-ray band also decreases with the increase of radial distance and the radial photon index remains roughly flat within the extended region to the edge of the remnant (Matheson & Safi-Harb 2005; Guest et al. 2019). The calculated results of the radial profiles of the photon index and surface brightness of the X-rays of the entire remnant in our model are shown in Figure 4, revealing that the radial profiles of the X-rays of the entire remnant, including the radial photon indices and surface brightness of the central PWN and the extended region, can also be well reproduced in the framework of our two-zone model.

3.1.3. Derived Parameters

With the pulsar and eject parameters of $T_{\rm age} = 870$ yr, $E_{\rm sn} = 1.0 \times 10^{51}$ erg and $M_{\rm ej} = 5.0\,M_{\odot}$, the dynamical radii of the PWN and the TS are derived to be $R_{\rm pwn}(T_{\rm age}) = 45\farcs4$ and $R_{\rm ts}(T_{\rm age}) = 2\farcs3$, respectively, consistent with the values of $R_{\rm pwn}(T_{\rm age}) = 40''$ and $R_{\rm ts}(T_{\rm age}) \geqslant 1\farcs5$ estimated by Slane et al. (2000). The ratios of the relevant quantities of electrons from the downstream of the TS are obtained to be $\gamma_{\rm b}/\Delta\gamma = 7$ and $\gamma_{\rm cut}/\Delta\gamma_{\rm cut} = 3$, and the high-energy tail carry about 6.8% of the kinetic energy in the downstream region of the TS, which are consistent with the results given by Spitkovsky (2008) and Sironi & Spitkovsky (2009). The total kinetic energy of all electrons injected from the PWN shock amounts to 9.8×10^{48} erg, which is about 0.98% of the total energy of the progenitor SN.

From the modeling results, the current magnetic field of G21.5-0.9 at the TS is derived to be $B_0(T_{\rm age}) = 15.6\ \mu$G, and the spatial average of the central PWN has a value of $\bar{B}(T_{\rm age}) = 36.1\ \mu$G, which is consistent with the spatially dependent model result of 43 μG given by Porth et al. (2016) and the one-zone spatially dependent model result of 37.7 μG of Lu et al. (2017b), but smaller than the values of 71 μG obtained by Torres et al. (2014) with a homogeneous model and 130 μG estimated by Guest et al. (2019) based on their pure diffusion model. The current magnetic field at the edge of the PWN is obtained to be 29.5 μG from our model. Then, the magnetic field in the extended region can be estimated to be 18.9 μG, according to the assumption that the magnetic field in the extended region is a ratio of the magnetic field at the edge

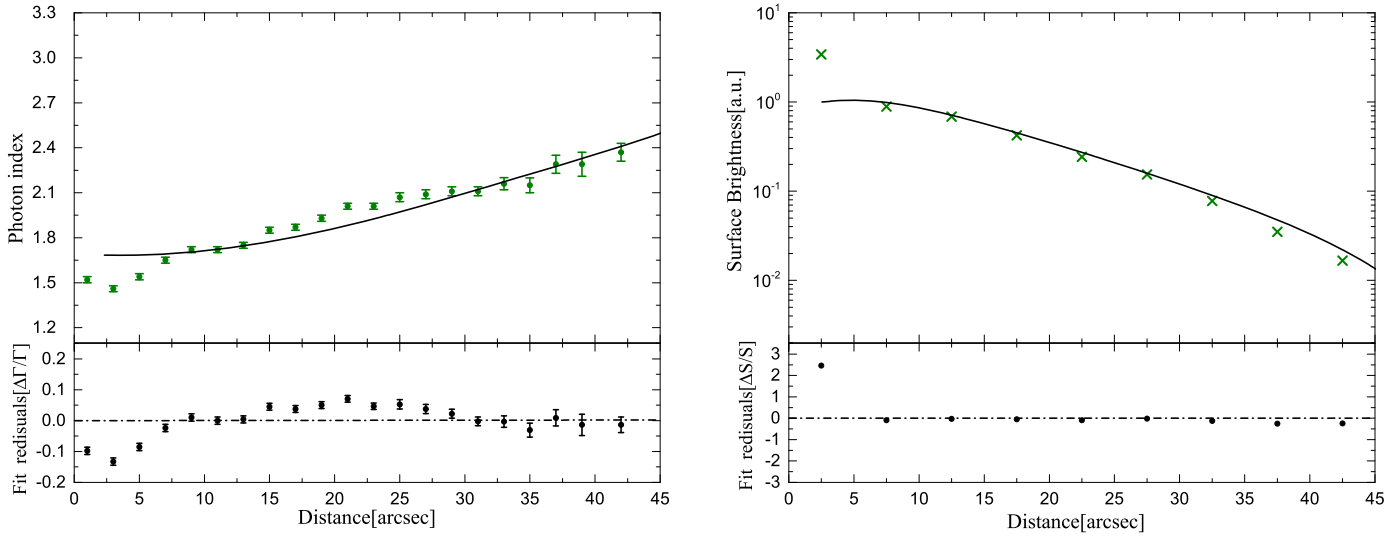

Figure 3. Comparison of the radial profiles of the photon index (left panel) and surface brightness (right panel) of the central PWN of G21.5-0.9 with the observed data at the X-ray band. The surface brightness are normalized as unity at the center. The radial photon index observed in the energy of 0.5–8 keV and the surface brightness observed in the 0.3–8 keV energy range are taken from Guest et al. (2019).

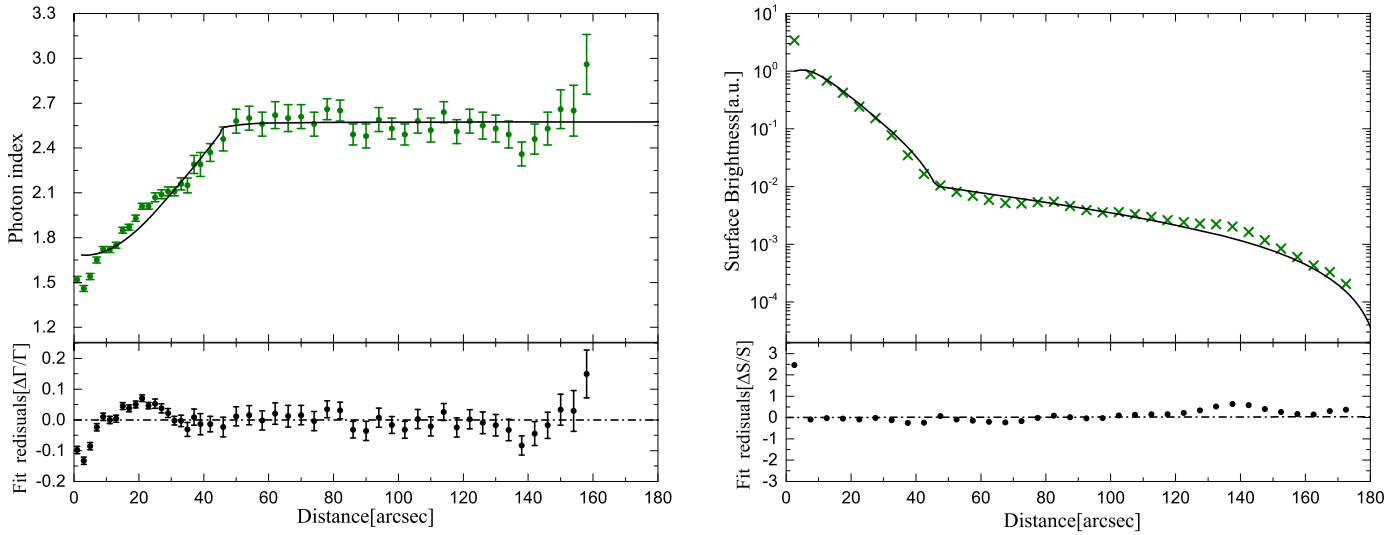

Figure 4. Same as Figure 3, but for the photon index (left panel) and surface brightness (right panel) of the entire remnant calculated with our two-zone model. The observed data are taken from Guest et al. (2019).

of the central nebula and a ratio of $\xi = 0.64$ is adopted in the framework of our model.

According to the adopted parameters listed in Table 1, the current particle diffusion coefficient at the TS is derived to be $\kappa_{0,1}(T_{\rm age}) = 5.7 \times 10^{25}\ {\rm cm^2\ s^{-1}}$ at an electron energy of 1 TeV, and the spatially averaged diffusion coefficient in the central nebula has a value of $\kappa_1(T_{\rm age}) = 2.5 \times 10^{25}\ {\rm cm^2\ s^{-1}}$, and that the diffusion coefficient in the extended region is obtained to be $\kappa_2(T_{\rm age}) = 1.7 \times 10^{28}\ {\rm cm^2\ s^{-1}}$. It should be noted that the spatially averaged diffusion coefficient of the central PWN obtained by our model is consistent with the value $2.1 \times 10^{25}\ {\rm cm^2\ s^{-1}}$ given by Vorster et al. (2013), but smaller than the values of 5.7×10^{26} and $2.1 \times 10^{27}\ {\rm cm^2\ s^{-1}}$ given by Porth et al. (2016) and Guest et al. (2019), respectively. Moreover, the value is larger than the result of $2.1 \times 10^{24}\ {\rm cm^2\ s^{-1}}$ obtained by Lu et al. (2017b), due to their study is focused on the central PWN and a free-escape boundary condition at the edge of the PWN is adopted. For the obtained diffusion coefficient of $1.7 \times 10^{27}\ {\rm cm^2\ s^{-1}}$ at 1 GeV in the extended region , which is smaller than the standard value $\sim 10^{28}\ {\rm cm^2\ s^{-1}}$ of the cosmic ray in the ISM given by Strong et al. (2007), but interesting consistent with the spiral arm model result of $\sim 10^{27}\ {\rm cm^2\ s^{-1}}$ estimated by Benyamin et al. (2014).

3.2. Comparisons with Other Models

In this section, our modeling results, especially for the radial profiles of the photon index and surface brightness in the X-ray band of the extended region, will be compared with the results of the two-zone pure diffusion model and the dust-scattering model of Bocchino et al. (2005), respectively.

3.2.1. Results of the Two-zone Pure Diffusion Model

The X-ray halo surrounding the central PWN of SNR G21.5-0.9, based on the XMM-*Newton* observations, is proposed to be an extension of the central synchrotron nebula (Warwick et al. 2001), i.e., the extended halo may be produced by synchrotron

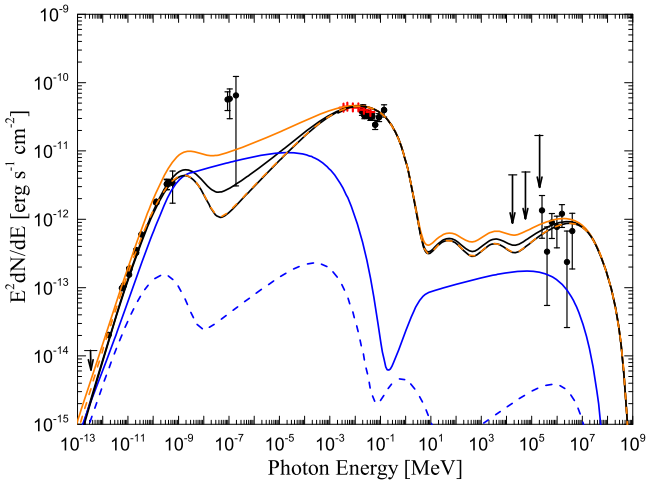

Figure 5. Same as Figure 2, but for the SEDs of the central PWN (black lines) and the extended region (blue lines) as well as the spectral flux of the entire remnant (orange lines) calculated with our two-zone model (solid lines) and the two-zone pure diffusion model (dash lines), respectively.

radiation of the particles diffuse from the central nebula. Here, the spatially radiative properties of the X-rays of the SNR G21.5-0.9 is also investigated in the framework of a two-zone pure diffusion model. In the model, the propagation and radiation of the particles in the remnant are the same as our two-zone model, but the particles of the extended region are only considered to be diffused from the central nebula. Then, the diffusion boundary condition, which is located at the edge of the PWN, can be transformed into

$$\kappa_1(r_b, \gamma, t)\frac{\partial n_e}{\partial r} = \kappa_2(r_b, \gamma, t)\frac{\partial n_e}{\partial r}, \quad (12)$$

where $r_b = R_{pwn}(t)$ is the position of the boundary and $R_{pwn}(t)$ is the radius of the PWN at time t.

The comparisons of the photon SEDs calculated in the two-zone pure diffusion model with those in our two-zone model as well as the observed data of G21.5-0.9 are shown in Figure 5. In the calculations, the values of the parameters are the same as those of our two-zone model except for the initial diffusion coefficient of the extended region. In the two-zone pure diffusion model, the initial diffusion coefficient is adopted to be 3.8×10^{21} cm^2 s^{-1} at 1 TeV. It can be seen from Figure 5 that the photon SED of the central PWN can be well reproduced in the framework of the two-zone pure diffusion model, but the spectral flux of the extended region is lower than that obtained by our two-zone model which includes the particles injected from the PWN shock.

The radial profiles of the photon index and surface brightness of the X-rays of the entire remnant calculated by the two-zone pure diffusion model are shown in Figure 6, indicating that the two-zone pure diffusion model can also well reproduce the radial photon index of the entire remnant. However, the radial surface brightness of the extended region in the X-ray band calculated by the two-zone pure diffusion model is much lower than the observed data given by Guest et al. (2019), which means that the X-rays of the extended region of G21.5-0.9 may be produced by the other origin particles, e.g., the particles derived from the PWN shock involved in our two-zone model.

3.2.2. Results of the Dust-scattering Model

Combined with *Chandra* and XMM-*Newton* observations, a self-consistent model is proposed to explain the X-ray observational features of SNR G21.5-0.9 (Bocchino et al. 2005). In this model, the X-ray halo consists of the diffuse extended emission due to the dust scattering of the X-rays from the central PWN, and the observational features of the radial surface brightness of the entire remnant can be explained well, but the radial variations of photon index of the X-rays was not investigated (Bocchino et al. 2005). To compare our modeling results with the results of the dust-scattering model, here the radial profiles of photon index and surface brightness of the X-rays of the extended region of G21.5-0.9 are calculated in the dust-scattering model of Predehl & Schmitt (1995).

In this paper, the distribution of the dust surrounding the nebula is assumed to be uniform and the analytical form of the differential cross section given by Draine (2003) is adopted for simplicity. Then, the halo spectral flux in an annulus of $\theta_1 < \theta < \theta_2$ can be calculated by (e.g., Posselt et al. 2015; Bîrzan et al. 2016)

$$F_{halo}(\theta_1, \theta_2, E) = F_C(E)\frac{\tau_{sca}(1\ \mathrm{keV})}{\Theta E}\mathcal{G}(\theta_1, \theta_2, E), \quad (13)$$

where E is the energy of the scattered photons, $F_C(E)$ is the flux of the central nebula, the constant Θ is adopted to be $\Theta = 360''$

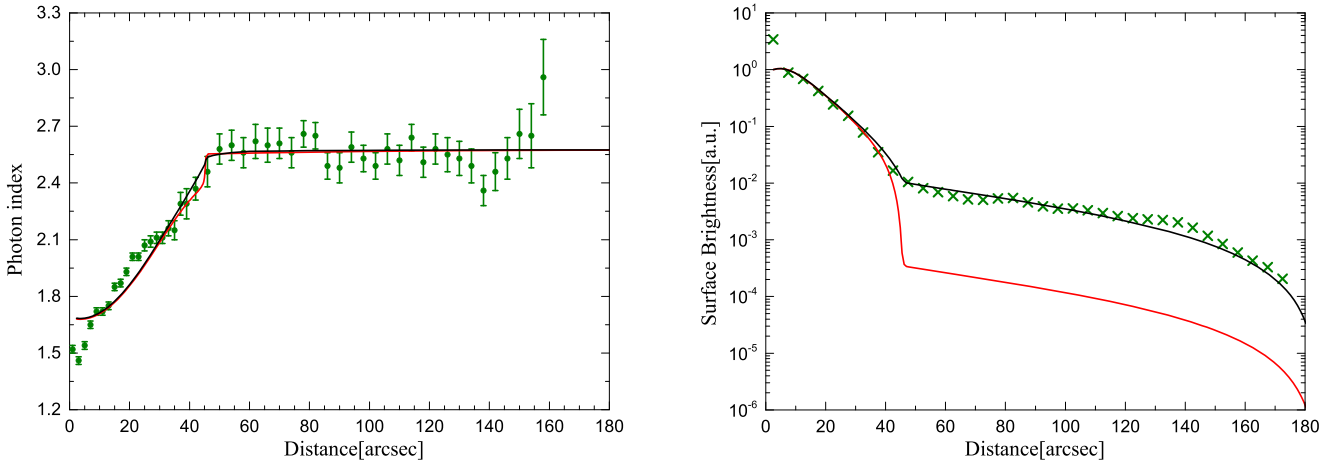

Figure 6. Same as Figure 4, but for the radial profiles of photon index (left panel) and surface brightness (right panel) of the entire remnant calculated with our two-zone model (black lines) and the two-zone pure diffusion model (red lines).

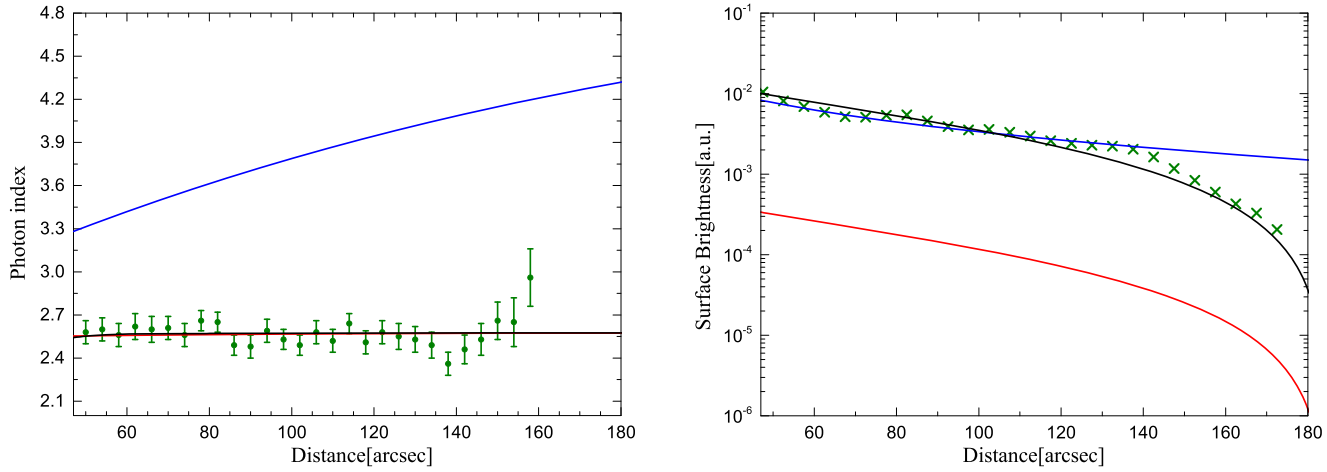

Figure 7. Radial profiles of photon index (left panel) and surface brightness (right panel) of the extended region of G21.5-0.9 calculated with our two-zone model (black lines), the two-zone pure diffusion model (red lines) and the dust-scattering model (blue lines).

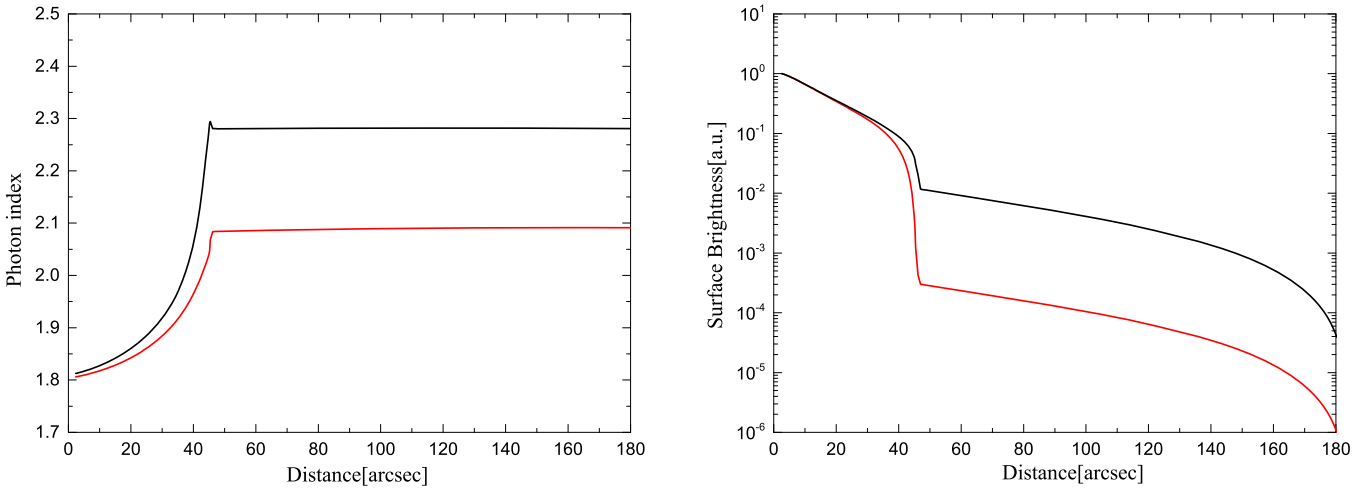

Figure 8. Radial profiles of photon index (left panel) and surface brightness (right panel) of the entire remnant of G21.5-0.9 in the energy range of 0.2–4 TeV calculated with our two-zone model (black lines) and the two-zone pure diffusion model (red lines). The surface brightness are normalized as unity at the center.

according to Draine (2003), $\tau_{\rm sca}(1\,{\rm keV})$ is the scattering optical width at 1 keV, and the function $\mathcal{G}(\theta_1, \theta_2, E) = [\theta_2 \arctan(\Theta/\theta_2 E) - \theta_1 \arctan(\Theta/\theta_1 E)]$.

The radial profiles of the photon index and surface brightness of the X-rays of the extended region calculated in the dust-scattering model are shown in Figure 7, where the values of the parameters of the central PWN are the same as our two-zone model and the parameter of $\tau_{\rm sca}(1\,{\rm keV})$ is chosen as 0.38. It can be seen from the right panel of Figure 7 that the radial surface brightness of the inner region of the extended region can be well reproduced in the framework of the dust-scattering model, but the surface brightness of the outer region is higher than the observations of Guest et al. (2019). Especially, from the left panel of Figure 7, it is obvious that the radial photon index of the extended region in the X-ray band cannot be well reproduced by the dust-scattering model. Therefore, combining with the modeling results given in Sections 3.1 and 3.2, it may be concluded that the X-ray halo of SNR G21.5-0.9 is mainly produced by the synchrotron radiation of the accelerated electrons injected from the PWN shock.

3.3. Radial Profiles of the TeV γ-Rays

The photon emission from the PWN of G21.5-0.9 has been detected at TeV γ-ray band (Djannati-Ataï et al. 2008), but the radial profiles of the photon index and the surface brightness of the SNR in the TeV band have not been reported in the literature. The TeV γ-ray properties of the central nebula have been spatially resolved in a particle transport model focusing on the bright central PWN, and the radial photon index of the TeV γ-rays in the central nebula is predicted to increase with the increase of radial distance (Lu et al. 2017b). In this paper, the radial profiles of the photon index and surface brightness of the entire remnant of G21.5-0.9 in the 0.2–4 TeV energy range are also calculated by our two-zone model with the adopted parameters listed in Table 1. Moreover, in order to investigate the contribution of TeV photons of the extended region from the particles diffuse from the central nebula, the radial profiles of the TeV γ-rays are also calculated in the two-zone pure diffusion model given in Section 3.2.1.

The calculated results of the radial profiles of the photon index and surface brightness of the entire remnant of SNR G21.5-0.9 in the energy range of 0.2–4 TeV are shown in Figure 8. It can be seen from the left panel of Figure 8 that the photon index of the central PWN in the TeV band also

increases with the increase of radial distance and becomes constant at ∼2.3 within the extended region in the framework our two-zone model, which is similar to the observed results of the X-rays, and that the radial photon index of the extended region predicted by the two-zone pure diffusion model is smaller than that obtained by our two-zone model. The radial surface brightness calculated with these two models are shown in the right panel of Figure 8, indicating that a faint TeV halo also surrounding the bright central PWN, which should be tested in the future observations. Moreover, the surface brightness of the extended region predicted by the two-zone pure diffusion model is lower than that obtained by our two-zone model, due to the particles injected from the PWN shock is considered in our model, which implies that the faint TeV halo is mainly due to the IC scattering of the particles injected from the PWN shock.

4. Summary and Discussion

In this paper, a two-zone spatially dependent model is presented to explain the observational features of SNR G21.5-0.9. In the model, the particle spectrum inside the entire remnant is described with the Fokker–Planck transport equation, the diffusion coefficient in the central PWN is smaller than that in the extended region, and the particles of the extended region originated from the central nebula and the PWN shock.

The photon SEDs, as well as the radial profiles of the photon index and surface brightness in the X-ray band of the central nebula and the extended region of SNR G21.5-0.9, have been calculated according to the parameters listed in Table 1, revealing that the observations can be well reproduced in the framework of our model (see Figures 2–4). The radial profiles of the photon index and surface brightness in the TeV band also have been studied in our model, and the photon index and surface brightness in the energy range of 0.2–4 TeV are predicted to also changes with the increasing radial distance, and the photon index varies from 1.8 in the core to 2.3 at the edge of the PWN and becomes a constant within the extended region, and the surface brightness of the entire remnant changes similar to that in the X-ray band (see Figure 8). Moreover, the current spatially averaged diffusion coefficient in the central PWN is derived to be $2.5 \times 10^{25}\,\mathrm{cm^2\,s^{-1}}$ at 1 TeV and the diffusion coefficient in the extended region has a value of $1.7 \times 10^{28}\,\mathrm{cm^2\,s^{-1}}$.

It has been proposed that the nonthermal X-ray halo of SNR G21.5-0.9 may be an extension of the central PWN (Warwick et al. 2001) or may be produced by the dust scattering of the X-rays from the central nebula (Bocchino et al. 2005). In this paper, the spatially radiative properties of G21.5-0.9 have been investigated in both the two-zone pure diffusion model and the dust-scattering model of Predehl & Schmitt (1995). From the modeling results, the radial profiles of the photon index of the entire remnant and the surface brightness of the central PWN can be well reproduced by the two-zone pure diffusion model, but the surface brightness of the extended region is lower than the observed data (see Figure 6). The calculated results given by the dust-scattering model indicated that the surface brightness of the inner region of the extended region can be well reproduced, but the radial photon index of the extended region is steeper than the observations (see Figure 7). Above all, we concluded that the surrounding X-ray halo of G21.5-0.9 is mainly due to the synchrotron radiation of the accelerated particles injected from the PWN shock.

Finally, the radial profiles of the photon index and surface brightness in the TeV band of the entire remnant of SNR G21.5-0.9 predicted by our model should be tested in the future observations. Furthermore, our two-zone model may also be suitable for the other composite SNRs, such as 3C58 and G54.1+0.3.

We thank the anonymous referee for the very constructive comments. This work is partially supported by National Key R & D Program of China under grant No. 2018YFA0404204, the National Natural Science Foundation of China (NSFC U1738211, 11433004, 11173020, 11803027), and the Yunnan local colleges applied basic research projects (2017FH001-17, 2017FH001-102).

ORCID iDs

Li Zhang https://orcid.org/0000-0002-7824-4289

References

Abeysekara, A. U., Albert, A., Alfaro, R., et al. 2017, Sci, 358, 911
Acero, F., Ackermann, M., Ajello, M., et al. 2013, ApJ, 773, 77
Acero, F., Aharonian, F., Akhperjanian, A. G., et al. 2010, A&A, 516, A62
Aguilar, M., Ali Cavasonza, L., Ambrosi, G., et al. 2016, PhRvL, 117, 231102
Atoyan, A. M., & Aharonian, F. A. 1996, MNRAS, 278, 525
Bamba, A., Yamazaki, R., Ueno, M., et al. 2003, ApJ, 589, 827
Becker, R. H., & Kundu, M. R. 1976, ApJ, 204, 427
Benyamin, D., Nakar, E., Piran, T., & Shaviv, N. J. 2014, ApJ, 782, 34
Bietenholz, M. F., & Bartel, N. 2008, MNRAS, 386, 1411
Bîrzan, L., Pavlov, G. G., & Kargaltsev, O. 2016, ApJ, 817, 129
Blondin, J. M., Chevalier, R. A., & Frierson, D. M. 2001, ApJ, 563, 806
Bocchino, F., van der Swaluw, E., Chevalier, R., & Bandiera, R. 2005, A&A, 442, 539
Bucciantini, N., Arons, J., & Amato, E. 2011, MNRAS, 410, 381
Bucciantini, N., Blondin, J. M., Del Zanna, L., & Amato, E. 2003, A&A, 405, 617
Caballero-Lopez, R. A., Moraal, H., McCracken, K. G., & McDonald, F. B. 2004, JGRA, 109, A12102
Camilo, F., Ransom, S. M., Gaensler, B. M., et al. 2006, ApJ, 637, 456
Caprioli, D., Amato, E., & Blasi, P. 2010a, APh, 33, 307
Caprioli, D., Kang, H., Vladimirov, A. E., & Jones, T. W. 2010b, MNRAS, 407, 1773
de Jager, O. C., & Djannati-Ataï, A. 2009, Astrophysics and Space Science Library, Vol. 1 (Berlin: Springer), 451
de Jager, O. C., & Harding, A. K. 1992, ApJ, 396, 161
de Rosa, A., Ubertini, P., Campana, R., et al. 2009, MNRAS, 393, 527
Djannati-Ataï, A., deJager, O. C., Terrier, R., Gallant, Y. A., & Hoppe, S. 2008, Proc. ICRC, (Merida, Mexico), 2, 823
Draine, B. T. 2003, ApJ, 598, 1026
Fang, J., Zhang, L., Zhang, J. F., Tang, Y. Y., & Yu, H. 2009, MNRAS, 392, 925
Gaensler, B. M., & Slane, P. O. 2006, ARA&A, 44, 17
Gallant, Y. A., Carrigan, S., Djannati-Ataï, A., et al. 2008, AIP Conf. Proc. 983, 40 Years of Pulsars: Millisecond Pulsars, Magnetars and More (Melville, NY: AIP), 195
Gallant, Y. A., & Tuffs, R. J. 1998, MmSAI, 69, 963
Ginzburg, V. L., & Syrovatskii, S. I. 1964, The Origin of Cosmic Rays (New York: Macmillan)
Goldreich, P., & Julian, W. H. 1969, ApJ, 157, 869
Guest, B. T., Safi-Harb, S., & Tang, X. 2019, MNRAS, 482, 1031
Holler, M., Schöck, F. M., Eger, P., et al. 2012, A&A, 539, A24
Kang, H., Ryu, D., & Jones, T. W. 2009, ApJ, 695, 1273
Kennel, C. F., & Coroniti, F. V. 1984a, ApJ, 283, 694
Kennel, C. F., & Coroniti, F. V. 1984b, ApJ, 283, 710
Kolb, C., Blondin, J., Slane, P., & Temim, T. 2017, ApJ, 844, 1
Lerche, I., & Schlickeiser, R. 1981, ApJS, 47, 33
Lu, F.-W., Gao, Q.-G., & Zhang, L. 2017a, ApJ, 834, 43
Lu, F.-W., Gao, Q.-G., Zhu, B.-T., & Zhang, L. 2017b, MNRAS, 472, 2926
Matheson, H., & Safi-Harb, S. 2005, AdSpR, 35, 1099

McKee, C. F. 1974, ApJ, 188, 335
Nynka, M., Hailey, C. J., Reynolds, S. P., et al. 2014, ApJ, 789, 72
Pacini, F., & Salvati, M. 1973, ApJ, 186, 249
Parker, E. N. 1965, P&SS, 13, 9
Porth, O., Vorster, M. J., Lyutikov, M., & Engelbrecht, N. E. 2016, MNRAS, 460, 4135
Posselt, B., Spence, G., & Pavlov, G. G. 2015, ApJ, 811, 96
Predehl, P., & Schmitt, J. H. M. M. 1995, A&A, 293, 889
Rees, M. J., & Gunn, J. E. 1974, MNRAS, 167, 1
Reynolds, S. P., & Chevalier, R. A. 1984, ApJ, 278, 630
Reynolds, S. P., Gaensler, B. M., & Bocchino, F. 2012, SSRv, 166, 231
Safi-Harb, S., Harrus, I. M., Petre, R., et al. 2001, ApJ, 561, 308
Salter, C. J., Reynolds, S. P., Hogg, D. E., Payne, J. M., & Rhodes, P. J. 1989, ApJ, 338, 171
Sironi, L., & Spitkovsky, A. 2009, ApJ, 698, 1523
Slane, P. 2017, Handbook of Supernovae (Cham: Springer), 2159
Slane, P., Chen, Y., Schulz, N. S., et al. 2000, ApJL, 533, L29
Slavin, J. D., Smith, R. K., Foster, A., et al. 2017, ApJ, 846, 77
Spitkovsky, A. 2008, ApJL, 682, L5
Strong, A. W., Moskalenko, I. V., & Ptuskin, V. S. 2007, ARNPS, 57, 285
Tanaka, S. J., & Takahara, F. 2011, ApJ, 741, 40
Tang, X., & Chevalier, R. A. 2012, ApJ, 752, 83
Torres, D. F., Cillis, A., Martín, J., & de Oña Wilhelmi, E. 2014, JHEAp, 1, 31
Truelove, J. K., & McKee, C. F. 1999, ApJS, 120, 299
Tsujimoto, M., Guainazzi, M., Plucinsky, P. P., et al. 2011, A&A, 525, A25
van der Swaluw, E., Achterberg, A., Gallant, Y. A., & Tóth, G. 2001, A&A, 380, 309
Vink, J., & Laming, J. M. 2003, ApJ, 584, 758
Vladimirov, A. E., Bykov, A. M., & Ellison, D. C. 2009, ApJL, 703, L29
Volpi, D., Del Zanna, L., Amato, E., & Bucciantini, N. 2008, A&A, 485, 337
Vorster, M. J., Tibolla, O., Ferreira, S. E. S., & Kaufmann, S. 2013, ApJ, 773, 139
Warwick, R. S., Bernard, J.-P., Bocchino, F., et al. 2001, A&A, 365, L248
Wilson, A. S., & Weiler, K. W. 1976, A&A, 53, 89
Zeng, H., Xin, Y., Liu, S., et al. 2017, ApJ, 834, 153
Zhang, L., Chen, S. B., & Fang, J. 2008, ApJ, 675, 21
Zhu, B.-T., Zhang, L., & Fang, J. 2018, A&A, 609, A110